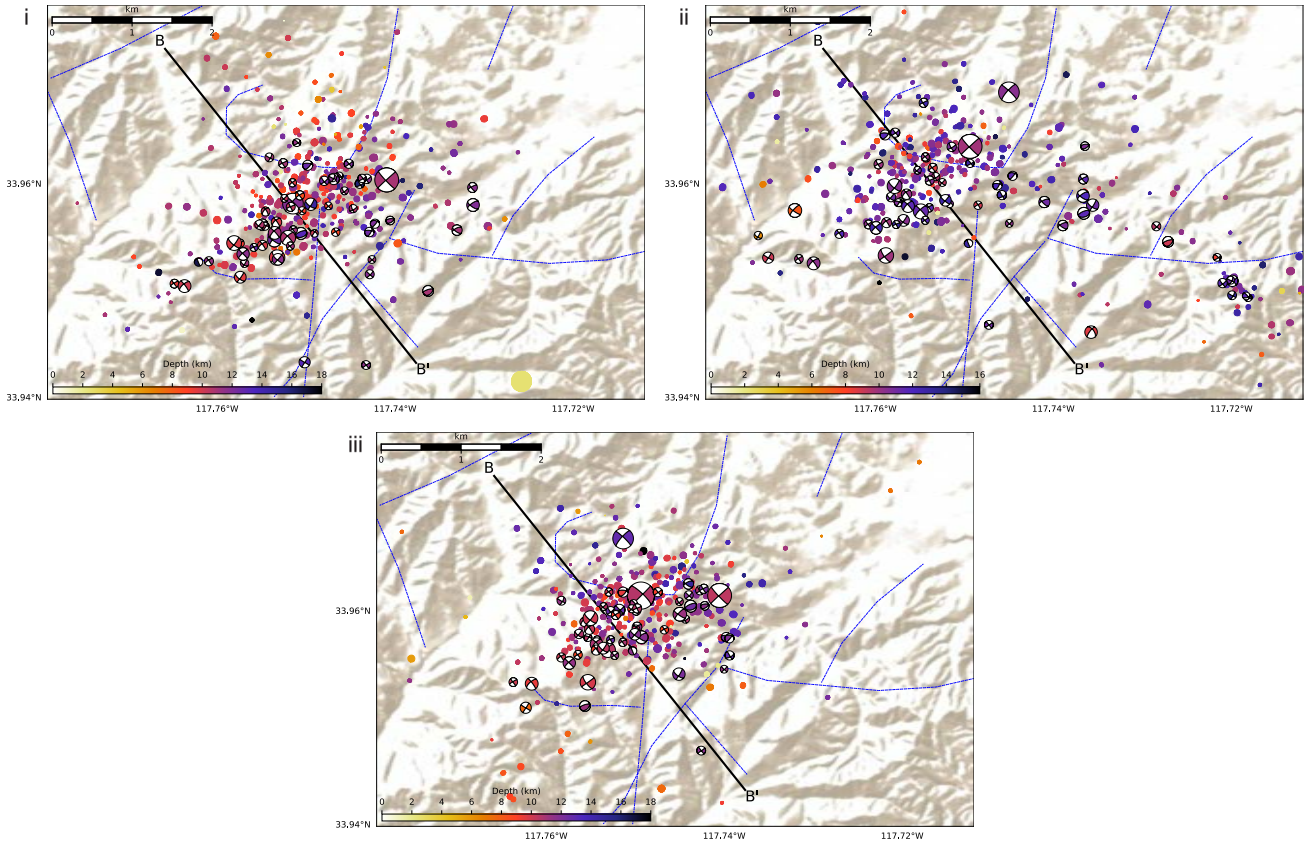

Figure 97: Relocated maps of the Chino Hills Sequence using a 0.6 RMS differential travel time residual and the three different velocity models. Figure 97-i shows the relocation results using the IASP91 velocity model. Figure 97-ii displays the relocation results using the smoothed southern California velocity model. Figure 97-iii are the relocation results from the LA Basin velocity model. Symbols as in Figure 55.

The IASP91 velocity model relocation results for the Chino Hills Sequence show a relatively narrow organization of events with some overall dispersion towards the northwest and the southeast (Figure 97-i). The northeast-southwest nodal plane of the strike-slip focal mechanism solutions show a similar orientation to that of the orientation of the overall sequence. (Figure 98). There is some deviation of events towards the southeast of the cross section at a depth of approximately 14 km. There also is an alignment of events near the middle of the cross section that extend upwards to about 4 km in depth and and downwards towards 18 km (Figure 98). Despite these small deviations, overall the relocation results for this velocity model at a 0.6 RMS parameter show a near-vertical orientation of events.

The smoothed southern California velocity model relocation results show a much more dispersed distribution of events compared to the other relocation results (Figure 97-ii). The most prominent feature of these results is the curved arrangements of events extending from the main assortment of the Chino Hills Sequence towards the southeast. In its entirety, this curved feature is made up of events in a separate cluster from the primary cluster (Figure 97). Whether or not this cluster is considered a part of the Chino Hills Sequence is questionable, but considering that the cluster intersects the eastern edge of the primary cluster as seen in Figure 76 is notable. The horizontal distribution at depth that was noted earlier is verified with the cross section analysis, where the sequence's horizontal distribution appears to be more expansive than previous relocation results (Figure 59-ii).

The LA Basin velocity model relocation results have the smallest distribution of events of the three relocation results (Figure 97-iii). However, the Chino Hills Sequence in these results do not have as much of a distribution along the northeast-southwest orientation as the other two results. Once again, the northeast-southwest nodal planes of the strike-slip focal mechanism solutions shown in this sequence correlate well with the overall orientation of the Chino Hills Sequence (Figure 97-iii). A notable feature within these results is the inclusion of a larger magnitude events that was not present in the other two

relocation results that had a 0.6 RMS differential travel time residual parameter. At depth, these events align themselves in a near-vertical orientation, similar to the other relocation results of both RMS parameters (Figure 98-iii). As stated previously, these relocated events produce the narrowest distribution of relocated events of the three relocation results for the 0.6 RMS differential travel time residual (Figure 98-iii).

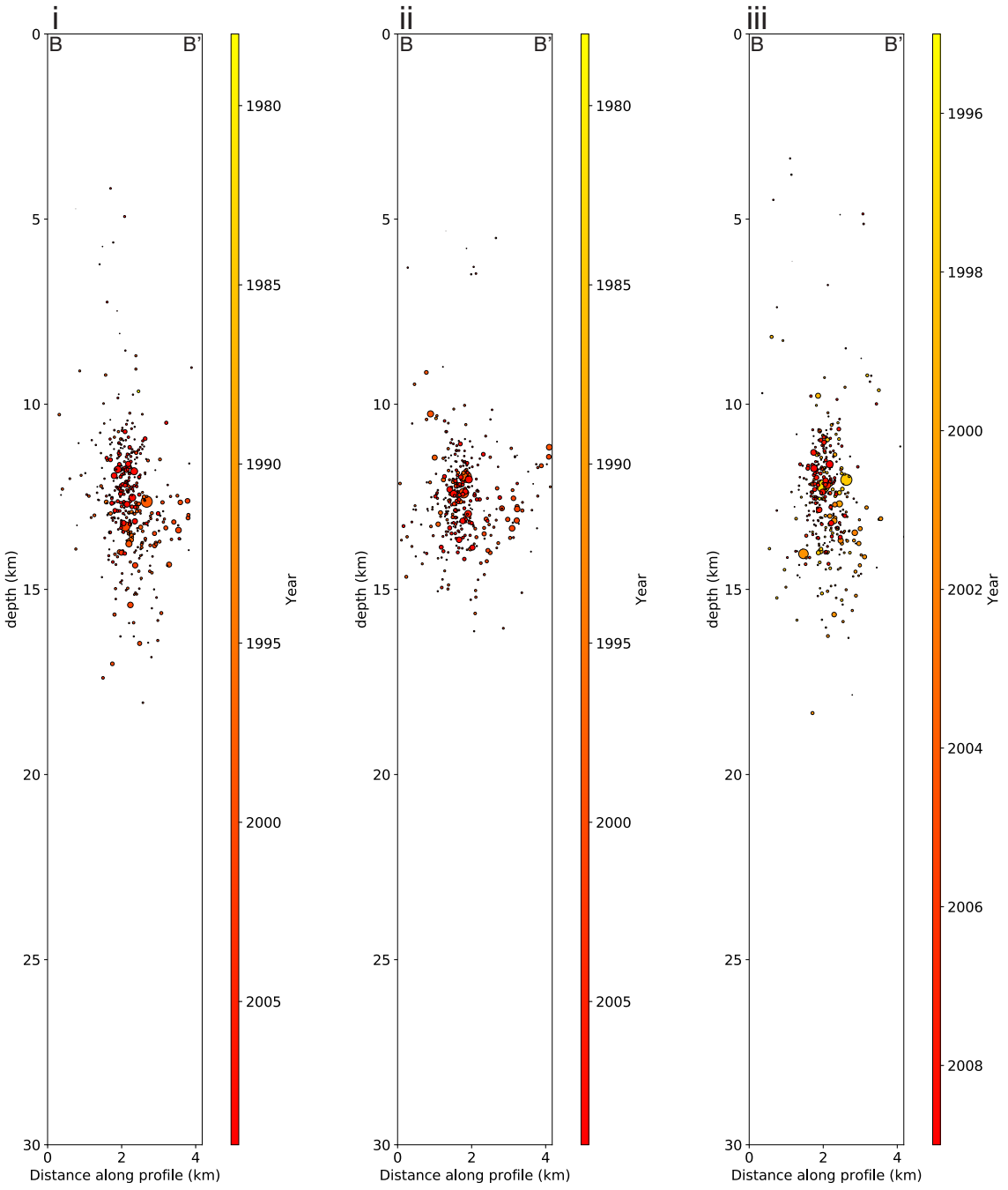

Figure 98: Cross sections illustrating each of the relocations of the Chino Hills Sequence using a 0.6 RMS differential travel time residual and the three different velocity models used. Figure 98-i shows the relocation results using the IASP91 velocity model. Figure 98-ii display the relocation results using the smoothed southern California velocity model. Figure 98-iii are the relocation results from the LA Basin velocity model.

The horizontal location errors for each of the velocity models show a similar trend: a large number of events with a horizontal error around 0.25 km with the number tapering

off significantly as the horizontal errors increase (Figure 99). However, these results also include a few events that have relatively large location errors. The spread of these errors is also the smallest, as indicated by the number of events within each standard deviation. The smallest average horizontal error is produced by the LA Basin velocity model relocation results, while also possessing the largest spread of horizontal errors (Figure 99-v).

The vertical errors of the Chino Hills Sequence share similarities on the distribution of the majority of events across all velocity model relocations (Figure 99). Unlike the horizontal errors, the smoothed southern California velocity model relocation results have the smallest overall vertical errors (Figure 99-iv). Similar to its horizontal errors, the LA Basin velocity model relocation results have the largest average vertical errors but do possess a smaller distribution of errors than the smoothed southern California model relocation results (Figure 99-vi).

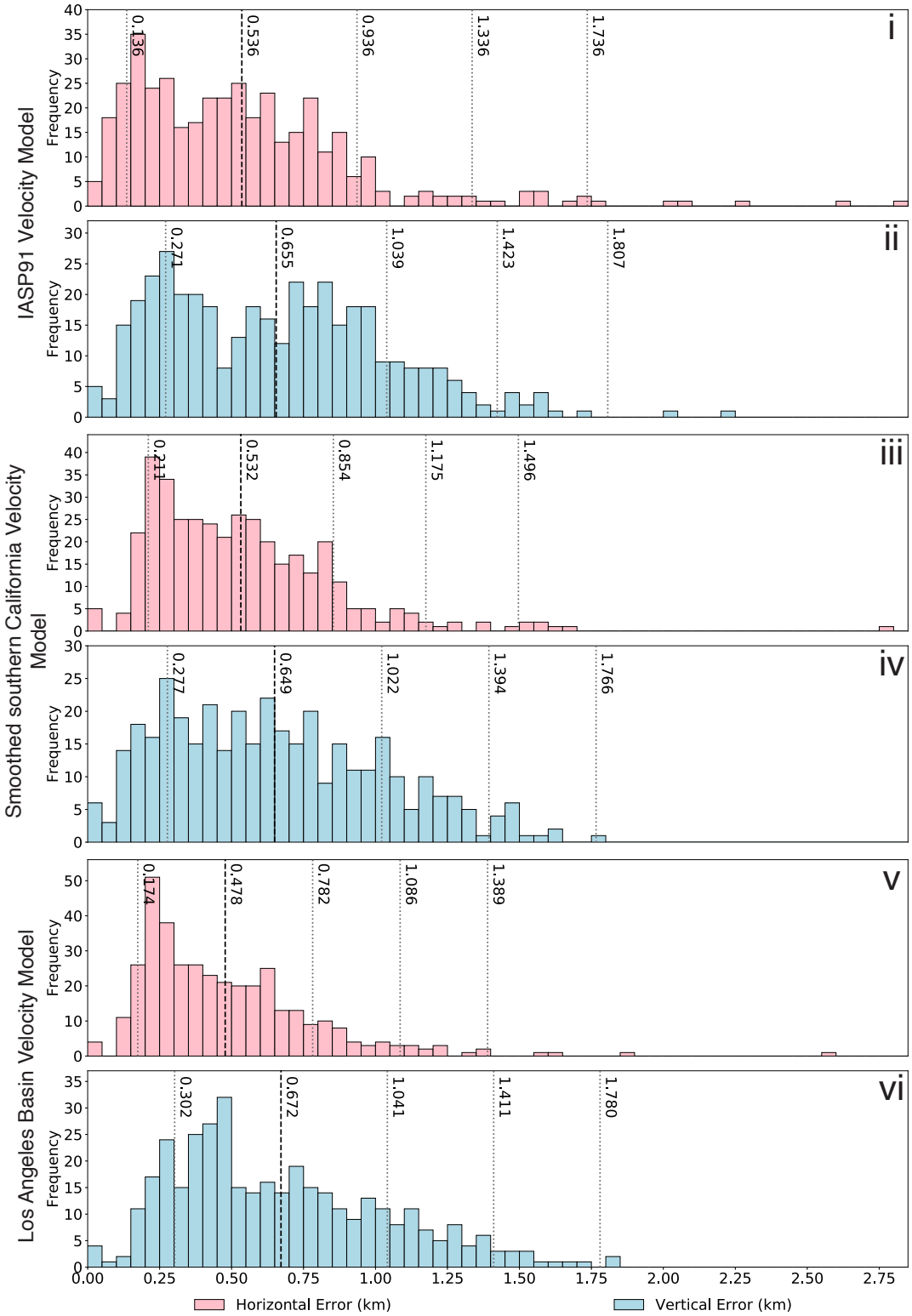

Figure 99: Histograms of the horizontal and vertical errors of the relocations for each velocity model of the Chino Hills Sequence, respectively. The black, dashed line indicates the average location error while the gray, dotted lines denote the standard deviations. Figure 99-i and 99-ii represent the IASP91 velocity model. Figure 99-iii and 99-iv represent the smoothed southern California velocity model. Figure 60-v and 99-vi represent Whittier Narrows velocity model.

The IASP91 relocation results contain the largest number of successfully relocated events and have a relatively well consolidated orientation, as well as the lowest horizontal errors of the three relocation results (Figure 97-i). The smoothed southern California velocity model results have the lowest number of relocated events, but have the best vertical errors. The location of the events is unusual in that the two clusters make up what appears to be two separate trends of events perpendicular to each other (Figure 97-ii). The LA Basin velocity model relocation results have the best visual relocation results, with the majority of the events forming a tight consolidation around northeast-southwest oriented trend (Figure 97-iii). These relocation results also have the lowest horizontal errors, but the worst vertical errors.

The IASP91 and LA Basin velocity model relocation results complement former studies on the 2008 Chino Hills earthquake in that the relocated events fall along a northeast-southwest oriented trend (Hauksson et al., 2008) (Figure 97-i, Figure 97-iii). Based on the strike-slip focal mechanisms present within the trend, this would indicate that these events ruptured along a left-lateral fault structure. This is further confirmed by the cross section views of these results; these events are aligned along a near-vertical trend (Figure 98-i, Figure 98-iii).

3.2.6 La Habra Sequence Relocation Results for all Velocity Models

The relocation results of all the velocity models for the La Habra Sequence bear similarities in certain aspects. The entire La Habra Sequence follows a northeast-southwest trend from the Whittier Fault towards the Coyote Hills Fault System (Figure 97). Each of the results have separated the events into two conglomerations: one on or near the Coyote Hills Fault System and one towards the middle-northeast portion of the trend (Figure 100). The majority of the events situated in the near vicinity of the Coyote Hills Fault System are strike-slip based on the focal mechanism solutions, while a large portion of the events within the center portion of the trend is a mixture of strike-slip

and reverse motion events.

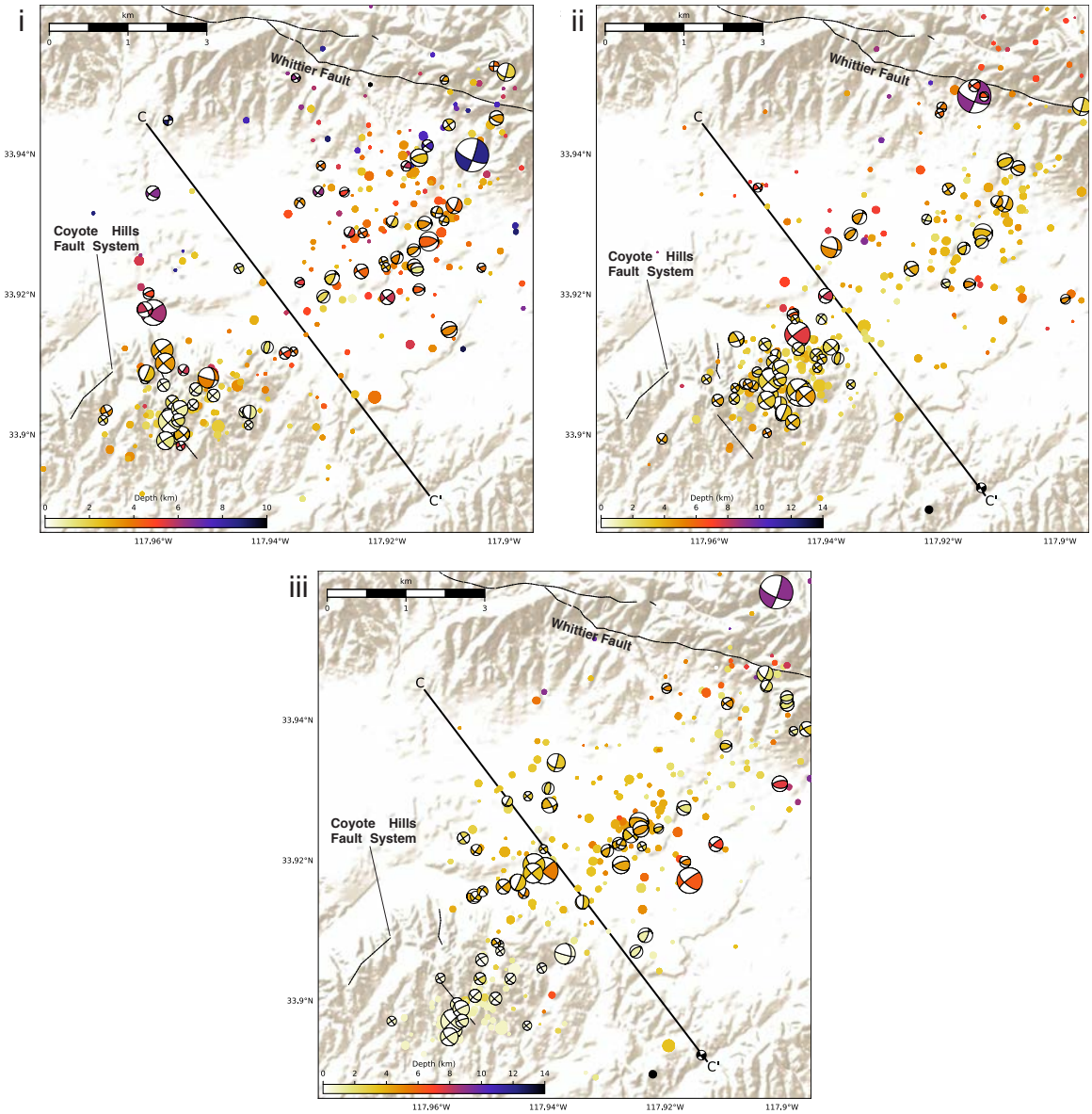

Figure 100: Relocated maps of the La Habra Sequence using a 0.6 RMS differential travel time residual and the three different velocity models used. Figure 100-i shows the relocation results using the IASP91 velocity model. Figure 100-ii display the relocation results using the smoothed southern California velocity model. Figure 100-iii are the relocation results from the LA Basin velocity model. Symbols as in Figure 55.

As mentioned before, the IASP91 velocity model relocation results show two distinct sets of events (Figure 114-i). The events situated near the Coyote Hills Fault System consist mainly of strike-slip events with a few reverse motion events scattered throughout. Many of the events within the clusters near the Coyote Hills Fault System are shallow in depth,

while events north of this series are deeper. The events making up the northeastern portion of the seismicity of the sequence consist of a mixture of strike-slip and reverse motion events all occurring at various depths throughout. A cross section view of these relocations shows an arrangement of events along what appears to be a near-vertical structure, with the consolidation of these events decreasing with an increase in depth.

The smoothed southern California velocity model relocation results also appear to be separated into two segments of seismicity, albeit the gap between these two segments is smaller than that of the IASP91 velocity model relocation results (Figure 100-ii). The southwestern most cluster is offset from the Coyote Hills Fault System with many of these events sitting at shallower depths. Based on the focal mechanisms observed, a large portion of the events making up the center segment of seismicity are reverse motion events with strike-slip events scattered throughout (Figure 100-ii). When looking at a cross section view of this sequence, these events appear to orient themselves around a steeply dipping fault structure extending down to 10 km (Figure 101-ii).

The LA Basin velocity model relocation results show an even more drastic view of seismicity making up the La Habra Sequence. While the relocations continue to have a break in seismicity, the gap is now prevalent in map view (Figure 100-iii) and in cross section view (Figure 101-iii). The shallower of these two segments transect the southern trace of the Coyote Hills Fault System, while the deeper of the two segments is located more towards the middle of the sequence. Overall, the relocations of the La Habra Sequence are more dispersed than those of the IASP91 and smoothed southern California velocity models, an observation that is strengthened by its cross section view, which shows two clear conglomerations of events along a near vertical structure (Figure 100-iii, Figure 101-iii). Because of their separation along the strike of the sequence as well as their separation at depth, it is possible that these two conglomerations may be along two separate faults as well.

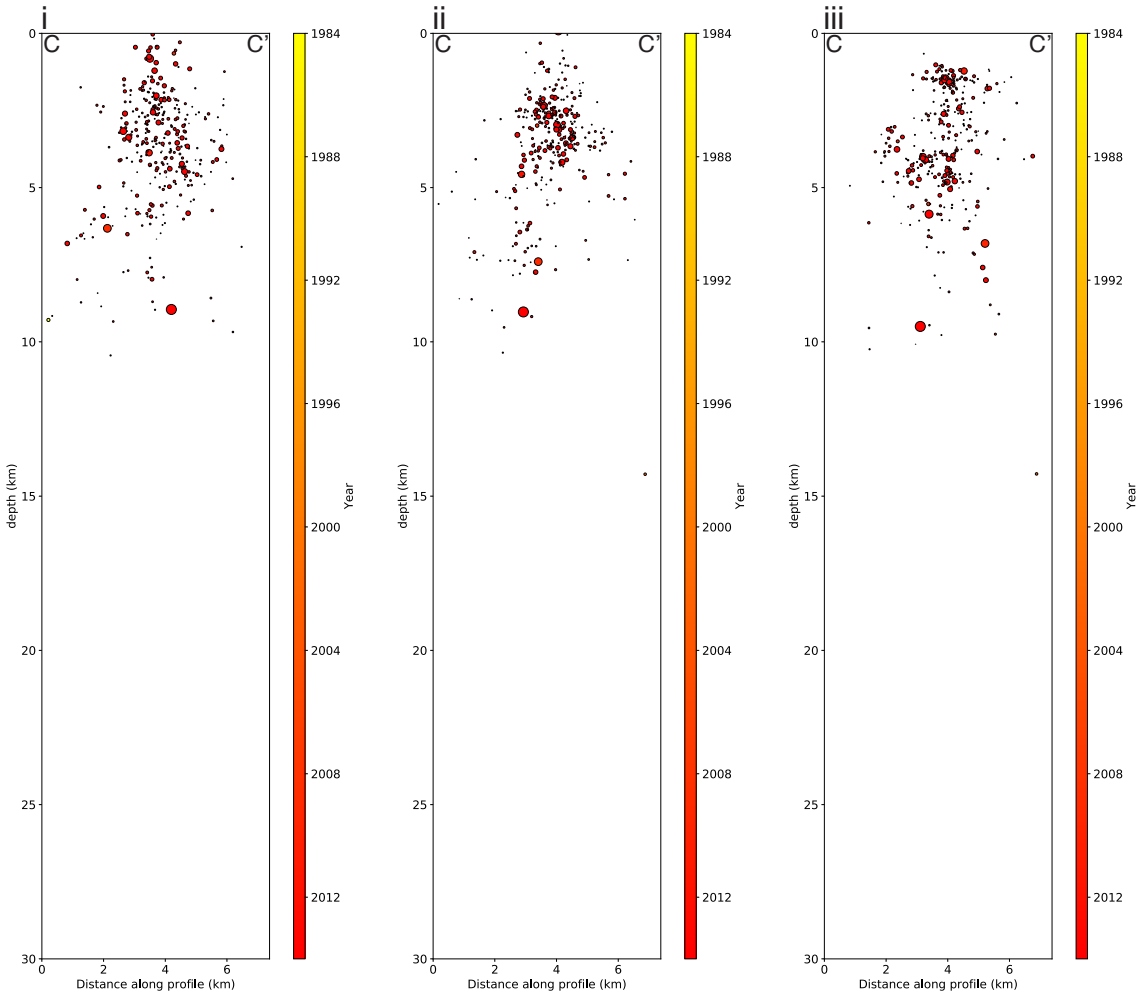

Figure 101: Cross sections illustrating each of the relocations of the La Habra Sequence using a 0.6 RMS differential travel time residual and the three different velocity models used. Figure 101-i shows the relocation results using the IASP91 velocity model. Figure 101-ii display the relocation results using the smoothed southern California velocity model. Figure 101-iii are the relocation results from the LA Basin velocity model.

The location errors for all the velocity models are similar to those of the 0.2 RMS differential travel time residual velocity model relocation results (Figure 102). The IASP91 velocity model relocation results have the smallest (though still large) average error and possess the smallest error distribution, whereas the LA Basin model relocation results possess the largest average error and distribution of the three results (Figure 102-i, Figure 102-v).

The vertical errors of the IASP91 and smoothed southern California velocity model relocation results are similar to those seen in the 0.2 RMS differential travel time residual

results, each having a high average error (0.888 and 0.812 km, respectively) (Figure 102-ii, Figure 102-iv). The spread on the IASP91 model relocations, however is considerably wider than that of the smoothed southern California model relocations. The LA Basin velocity model relocation results, however have a significantly smaller average error and distribution than all other relocation results presented (Figure 102-vi). This could be due to the number of P- and S-waves used to relocate the events within the La Habra Sequence, which is higher than for all other relocation results.

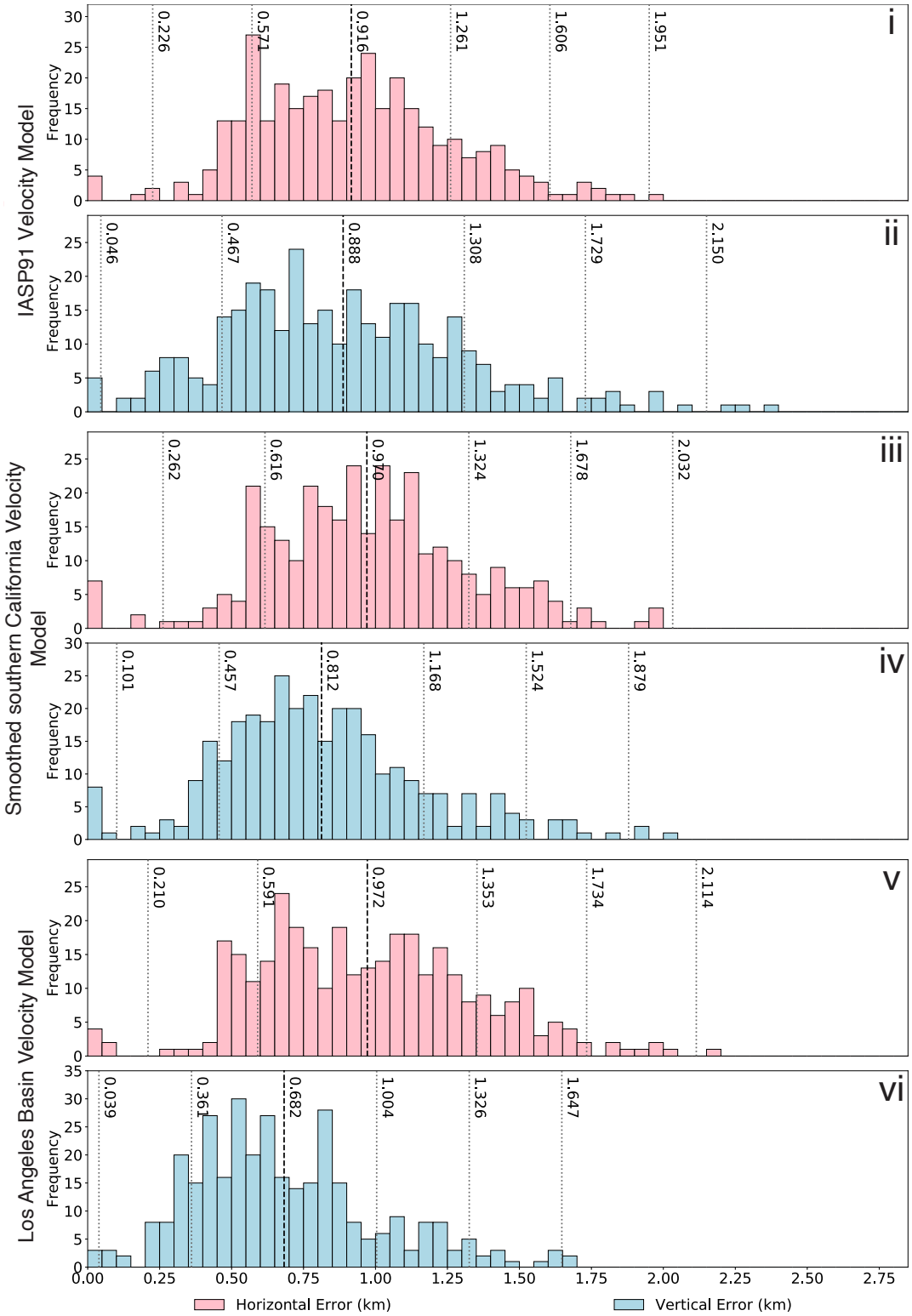

Figure 102: Histograms of the horizontal and vertical errors of the relocations for each velocity model of the La Habra Sequence, respectively. The black, dashed line indicates the average location error while the gray, dotted lines denote the standard deviations. Figure 102-i and 102-ii represent the IASP91 velocity model. Figure 102-iii and 102-iv represent the smoothed southern California velocity model. Figure 63-v and 102-vi represent Whittier Narrows velocity model.

As discussed with the 0.2 RMS differential travel time residual results for the La Habra Sequence, the La Habra mainshock and aftershock sequence were determined to be situated along a steeply dipping left-lateral strike-slip fault (Donnellan et al., 2015). It is clear that these events do consolidate around a somewhat linear feature extending from the Whittier Fault towards the Coyote Hills Fault System, indicating a left-lateral strike-slip fault (Figure 100). However, only the smoothed southern California velocity model relocation results shows in some part a steeply dipping structure. The other two relocation results have these events clustered around a near-vertical structure (Figure 62). However, the location errors of these results imply that these relocations are not very accurate and we do not have a high level of confidence in the presence of this dipping structure.

4 Conclusions

To better illuminate the potential fault structure(s) associated with the seismicity of the Yorba Linda Trend, the La Habra Sequence and surrounding areas, we applied a waveform cross-correlation technique to compare waveforms and generate improved arrival time measurements for P- and S-waves and subsequently entered these data into the GrowClust relative relocation algorithm. We used three different velocity models in our analysis and interpret the results for two different RMS differential travel time residuals of 0.2 s and 0.6 s.

All relocation results consistently indicate that both the Yorba Linda and Chino Hills Sequences are produced by northeast-southwest striking faults with a near-vertical or very steep dip. In combination with the focal mechanisms for the larger earthquakes in the Yorba Linda Sequence, we conclude that the motion along this structure is left-lateral strike-slip, with the fault striking at approximately 75°to the Whittier Fault surface trace. There is variability in the different relocation results on whether the Yorba Linda Sequence crosses the Whittier Fault; some results indicates that the sequence crosses the Whittier Fault, while others do not. We interpret the Chino Hills Sequence in a similar way, in that it also is produced by a left-lateral strike-slip fault. The presence of pure reverse motion events surrounding the Chino Hills Sequence may imply several smaller faults within this region that exhibit a reverse motion. The lack of relocated events between these two sequences would indicate that there is no definitive single through-going fault connecting the two sequences.

Relocations of the La Habra Sequence consistently reveal that these events are oriented along a northeast-southwest striking fault, beginning at the Whittier Fault and extending towards the Coyote Hills Fault System. This orientation, in combination with the focal mechanisms of this sequence, would imply the existence of a left-lateral strike-slip fault. The relocations show mixed results on the dip of this structure. Two of the relocation results for the 0.2 RMS differential travel time residual, as well as one of the

results for the 0.6 RMS differential travel time residual, show a steeply dipping feature, while the remaining relocation results indicate a near-vertical structure. Other interesting observations include the clustering of events southwest from the Yorba Linda Sequence, in the area of the Richfield Oil Field, which may point to a possible anthropogenic source.

Based on all of the relocation results presented, we do not see a definitive through-going fault connecting the major sequences within the Yorba Linda Trend, rather the Yorba Linda and Chino Hills Sequences likely occur on separate faults. Furthermore, we do not see any seismicity trends that imply the presence of bookshelf faulting that connect the two sequences.

5 Suggestions for Future Work

Future research into the seismicity of this region could use a 3D velocity model such as the SCEC Unified Community Velocity Model (UCVM) (Small et al., 2017) as an improvement over the 1D velocity models that were used in this research. The use of a 3D velocity model incorporates lateral changes in velocity in addition to changes in velocity with depth, thus correcting for small regional differences. In addition, the number of iterative bootstraps used to relocate event could be increased significantly, allowing for more robust relocations and potentially decreasing the location errors that were presented.

Another step before proceeding to relative relocation would be to use an absolute location program such as HypoInverse to further refine the precise absolute locations of earthquakes prior to relocating the events relative to each other. In tandem with the absolute location algorithms, the use of a different relocation algorithm, such as Bayesloc, might provide alternative results for further comparison (Myers et al., 2010).

Aside from relocation methods that may be applied or improved upon, near-surface geophysical methods including magnetic surveys or resistivity can be utilized to determine if a complete through-going fault or a series of faults are present in the area encompassing the Yorba Linda Trend.

References

Astiz, L., Shearer, P. M., & Agnew, D. C. (2000). Precise relocations and stress change calculations for the upland earthquake sequence in southern California. *Journal of Geophysical Research: Solid Earth*, *105*(B2), 2937–2953.

Atwater, T. M. (1998). Plate tectonic history of southern California with emphasis on the western Transverse Ranges and northern Channel Islands.

Baldwin, J. N., Kelson, K. I., & Randolph, C. E. (2000). Late Quaternary fold deformation along the Northridge Hills Fault, Northridge, California: Deformation coincident with past Northridge blind-thrust earthquakes and other nearby structures? *Bulletin of the Seismological Society of America*, *90*(3), 629–642.

Bjorklund, T., & Burke, K. (2002). Four-dimensional analysis of the inversion of a half-graben to form the Whittier fold–fault system of the Los Angeles Basin. *Journal of Structural Geology*, *24*(9), 1369–1387.

Bjorklund, T., Burke, K., Zhou, H.-w., & Yeats, R. S. (2002). Miocene rifting in the Los Angeles Basin: Evidence from the Puente Hills half-graben, volcanic rocks, and P-wave tomography. *Geology*, *30*(5), 451–454.

Chen, P., Jordan, T. H., & Zhao, L. (2005). Finite-moment tensor of the 3 September 2002 Yorba Linda earthquake. *Bulletin of the Seismological Society of America*, *95*(3), 1170–1180.

Chen, P., Jordan, T. H., & Zhao, L. (2010). Resolving fault plane ambiguity for small earthquakes. *Geophysical Journal International*, *181*(1), 493–501.

Crotwell, H. P., Owens, T. J., & Ritsema, J. (1999). The TauP Toolkit: Flexible seismic travel-time and ray-path utilities. *Seismological Research Letters*, *70*, 154–160.

Darin, M. H., & Dorsey, R. J. (2013). Reconciling disparate estimates of total offset on the southern San Andreas Fault. *Geology*, *41*(9), 975–978.

Donnellan, A., Grant Ludwig, L., Parker, J. W., Rundle, J. B., Wang, J., Pierce, M., ... Hensley, S. (2015). Potential for a large earthquake near Los Angeles inferred from

the 2014 La Habra earthquake. *Earth and Space Science*, *2*(9), 378–385.

Hauksson, E. (1990). Earthquakes, faulting, and stress in the Los Angeles Basin. *Journal of Geophysical Research: Solid Earth*, *95*(B10), 15365–15394.

Hauksson, E., Felzer, K., Given, D., Giveon, M., Hough, S., Hutton, K., ... Yong, A. (2008). Preliminary report on the 29 July 2008 Mw 5.4 Chino Hills, eastern Los Angeles Basin, California, earthquake sequence. *Seismological Research Letters*, *79*(6), 855–866.

Hauksson, E., Göbel, T., Ampuero, J.-P., & Cochran, E. (2015). A century of oil-field operations and earthquakes in the greater Los Angeles Basin, southern California. *The Leading Edge*, *34*(6), 650–656.

Hauksson, E., Hutton, K., Jones, L., & Given, D. (2002). *2002/09/03 M4.6 Yorba Linda.* California Institute of Technology. Retrieved from `https://www.scsn.org/index.php/earthquakes/speqrep/20020903-m4-6-yorba-linda/index.html`

Hauksson, E., & Jones, L. M. (1989). The 1987 Whittier Narrows earthquake sequence in Los Angeles, southern California: Seismological and tectonic analysis. *Journal of Geophysical Research: Solid Earth*, *94*(B7), 9569–9589.

Hauksson, E., & Shearer, P. (2005). Southern California hypocenter relocation with waveform cross-correlation, part 1: Results using the double-difference method. *Bulletin of the Seismological Society of America*, *95*(3), 896–903.

Hauksson, E., Yang, W., & Shearer, P. M. (2012). Waveform relocated earthquake catalog for southern California (1981 to June 2011). *Bulletin of the Seismological Society of America*, *102*(5), 2239–2244.

Hutton, K., Woessner, J., & Hauksson, E. (2010). Earthquake monitoring in southern California for seventy-seven years (1932–2008). *Bulletin of the Seismological Society of America*, *100*(2), 423–446.

Jennings, C. W., Bryant, W. A., & Saucedo, G. (2010). Fault activity map of California.

California Geological Survey Geologic Data Map, *6*.

Kennett, B., & Engdahl, E. (1991). Traveltimes for global earthquake location and phase identification. *Geophysical Journal International*, *105*(2), 429–465.

Lin, G., Shearer, P. M., & Hauksson, E. (2007). Applying a three-dimensional velocity model, waveform cross correlation, and cluster analysis to locate southern California seismicity from 1981 to 2005. *Journal of Geophysical Research: Solid Earth*, *112*(B12).

Luyendyk, B. P. (1991). A model for Neogene crustal rotations, transtension, and transpression in southern California. *Geological Society of America Bulletin*, *103*(11), 1528–1536.

Luyendyk, B. P., Kamerling, M. J., & Terres, R. (1980). Geometric model for Neogene crustal rotations in southern California. *Geological Society of America Bulletin*, *91*(4), 211–217.

Matoza, R. S., Shearer, P. M., Lin, G., Wolfe, C. J., & Okubo, P. G. (2013). Systematic relocation of seismicity on Hawaii Island from 1992 to 2009 using waveform cross correlation and cluster analysis. *Journal of Geophysical Research: Solid Earth*, *118*(5), 2275–2288.

Mori, J. (1993). Fault plane determinations for three small earthquakes along the San Jacinto Fault, California: Search for cross faults. *Journal of Geophysical Research: Solid Earth*, *98*(B10), 17711–17722.

Myers, S. C., Johannesson, G., & Simmons, N. A. (2010). *Bayesloc multiple-event location applied to a global data set* (Tech. Rep.). LAWRENCE LIVERMORE NATIONAL LAB CA.

Nicholson, C., Seeber, L., Williams, P., & Sykes, L. R. (1986). Seismicity and fault kinematics through the eastern Transverse Ranges, California: Block rotation, strike-slip faulting and low-angle thrusts. *Journal of Geophysical Research: Solid Earth*, *91*(B5), 4891–4908.

Olsen, K. B., & Mayhew, J. E. (2010). Goodness-of-fit criteria for broadband synthetic seismograms, with application to the 2008 Mw 5.4 Chino Hills, California, earthquake. *Seismological Research Letters*, *81*(5), 715–723.

Richards-Dinger, K., & Shearer, P. (2000). Earthquake locations in southern California obtained using source-specific station terms. *Journal of Geophysical Research: Solid Earth*, *105*(B5), 10939–10960.

Ross, Z. E., Idini, B., Jia, Z., Stephenson, O. L., Zhong, M., Wang, X., ... others (2019). Hierarchical interlocked orthogonal faulting in the 2019 Ridgecrest earthquake sequence. *Science*, *366*(6463), 346–351.

(SCEDC), S. C. E. D. C. (2013). Southern California Earthquake Center. *Caltech. Dataset*.

Schaff, D. P., & Waldhauser, F. (2005). Waveform cross-correlation-based differential travel-time measurements at the Northern California Seismic Network. *Bulletin of the Seismological Society of America*, *95*(6), 2446–2461.

Shao, G., Ji, C., & Hauksson, E. (2012). Rupture process and energy budget of the 29 July 2008 Mw 5.4 Chino Hills, California, earthquake. *Journal of Geophysical Research: Solid Earth*, *117*(B7).

Shearer, P. M. (1997). Improving local earthquake locations using the L1 norm and waveform cross correlation: Application to the Whittier Narrows, California, aftershock sequence. *Journal of Geophysical Research: Solid Earth*, *102*(B4), 8269–8283.

Small, P., Gill, D., Maechling, P. J., Taborda, R., Callaghan, S., Jordan, T. H., ... Goulet, C. (2017). The SCEC unified community velocity model software framework. *Seismological Research Letters*, *88*(6), 1539–1552.

Stein, S., & Wysession, M. (2009). *An introduction to seismology, earthquakes, and earth structure*. John Wiley & Sons.

Thompson, G., & Reyes, C. (2018). *GISMO a seismic data analysis toolbox for MATLAB [software package].*

Trugman, D. T. (2017a). *Deviant earthquakes: Data-driven constraints on the variability in earthquake source properties and seismic hazard* (Unpublished doctoral dissertation). UC San Diego.

Trugman, D. T. (2017b). Growclust: A computer program for the relative relocation of earthquake hypocenters user guide, version 1.1.

Trugman, D. T., & Shearer, P. M. (2017). Growclust: A hierarchical clustering algorithm for relative earthquake relocation, with application to the Spanish Springs and Sheldon, Nevada, earthquake sequences. *Seismological Research Letters*, *88*(2A), 379–391.

Waldhauser, F., & Schaff, D. P. (2008). Large-scale relocation of two decades of northern California seismicity using cross-correlation and double-difference methods. *Journal of Geophysical Research: Solid Earth*, *113*(B8).

Walls, C., Rockwell, T., Mueller, K., Bock, Y., Williams, S., Pfanner, J., ... Fang, P. (1998). Escape tectonics in the Los Angeles metropolitan region and implications for seismic risk. *Nature*, *394*(6691), 356.

Yang, W., Hauksson, E., & Shearer, P. M. (2012). Computing a large refined catalog of focal mechanisms for southern California (1981–2010): Temporal stability of the style of faulting. *Bulletin of the Seismological Society of America*, *102*(3), 1179–1194.

Yeats, R. S. (2004). Tectonics of the San Gabriel Basin and surroundings, southern California. *GSA Bulletin*, *116*(9-10), 1158–1182.

6 Appendix

6.1 Appendix A: Original Event Locations for Each Velocity Model Relocation Results with a 0.2 RMS Differential Travel Time Residual

Shown below are maps of all original locations of events that were to be relocated using the three different velocity models under a 0.2 RMS differential travel time residual parameter used in this study. Figures 103, 104, and 105 show the original event locations the IASP91, for the smoothed southern California and Los Angeles Basin velocity models , respectively.

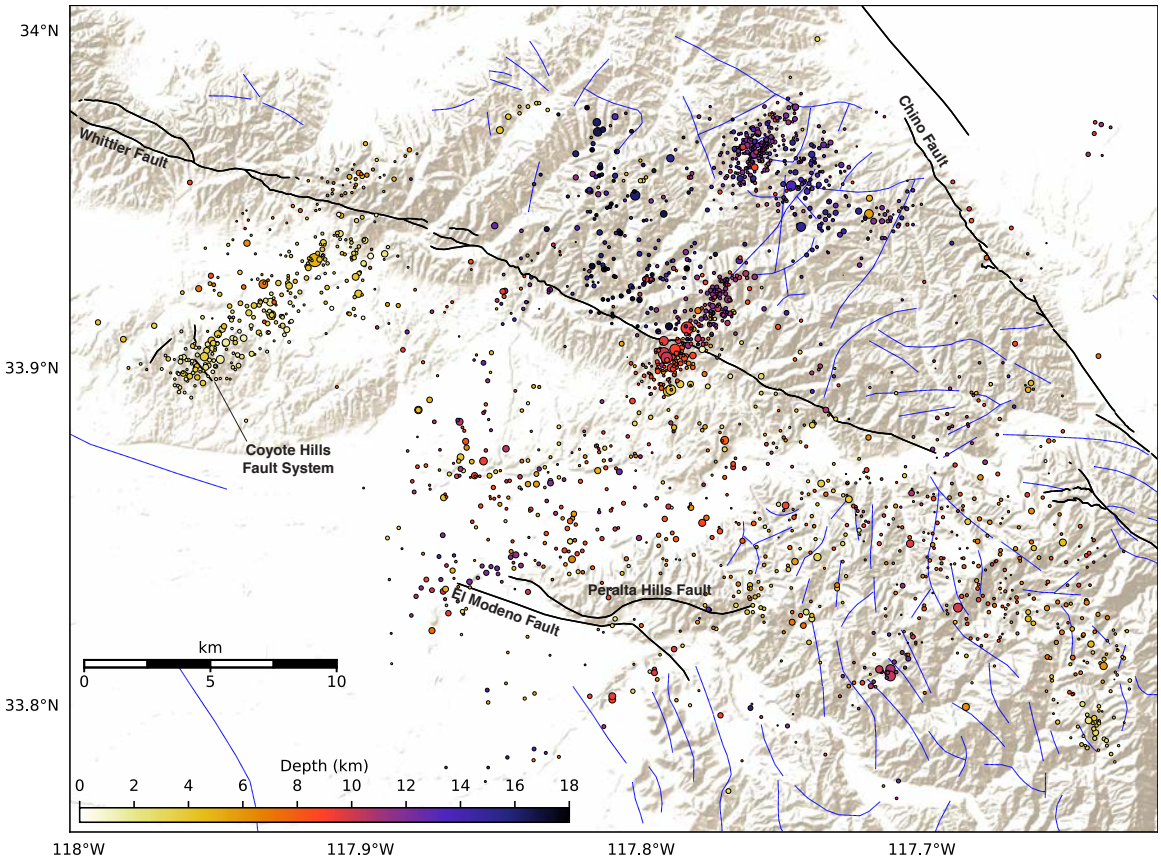

Figure 103: Map of the original events of events shown in Figure 106 using a 0.2 differential travel time residual and the Smoothed Southern California Velocity Model (Figure 23a).

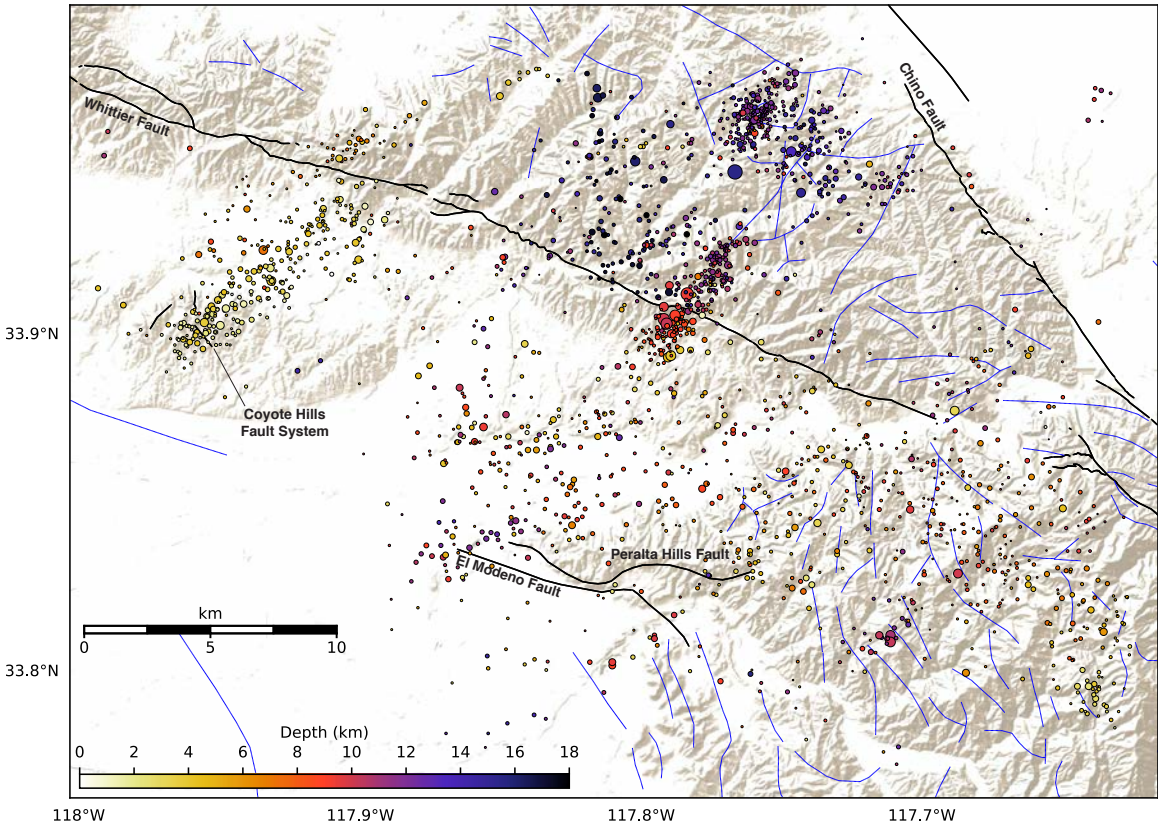

Figure 104: Map of the original locations of events shown in Figure 107 using a 0.2 differential travel time residual and the Smoothed Southern California Velocity Model (Figure 23b).

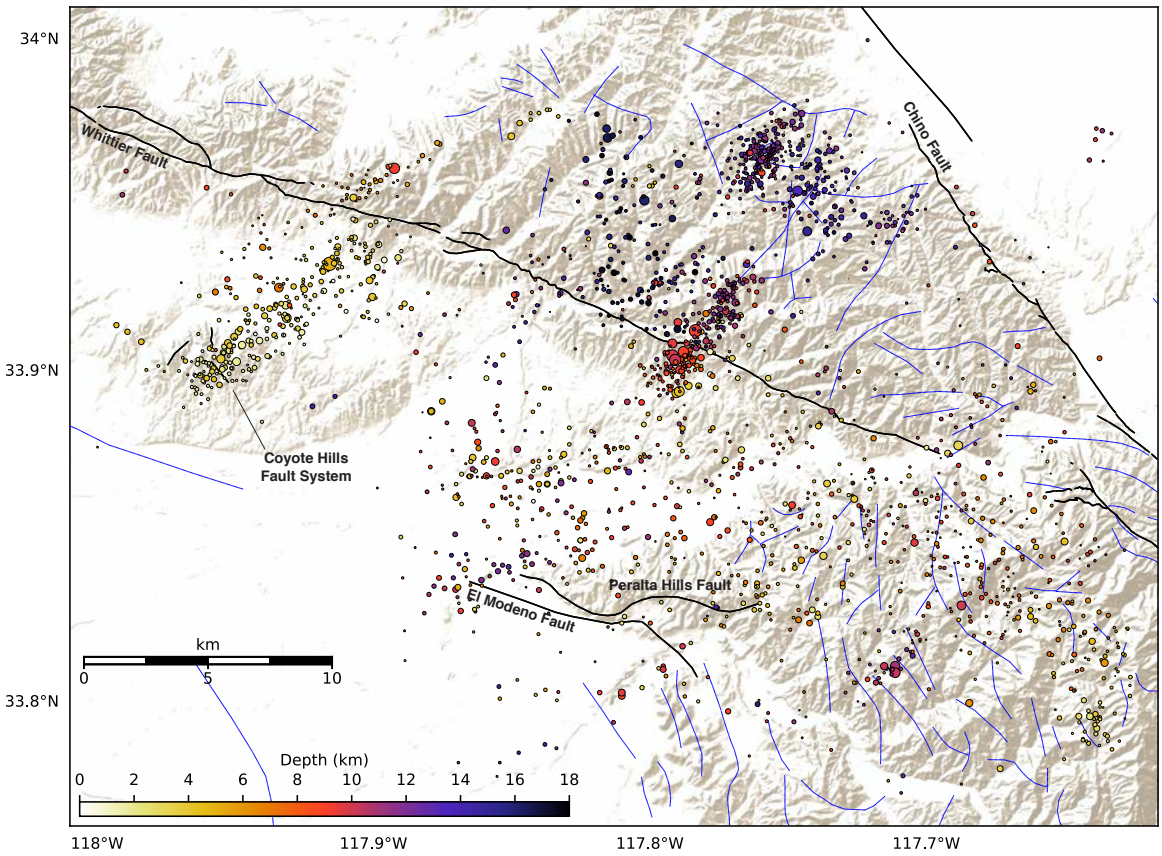

Figure 105: Map of the original events of events shown in Figure 108 using a 0.2 differential travel time residual and the 1987 Whittier Narrows Earthquake Velocity Model (Figure 23c).

6.2 Appendix B: Relocated Event Locations for Each Velocity Model Relocation Results with a 0.2 RMS Differential Travel Time Residual

Shown below are maps of all relocated event locations of events for the three different velocity models under a 0.2 RMS differential travel time residual parameter used in this study. Figures 106, 107, and 108 show the relocated event locations the IASP91, for the smoothed southern California and Los Angeles Basin velocity models , respectively.

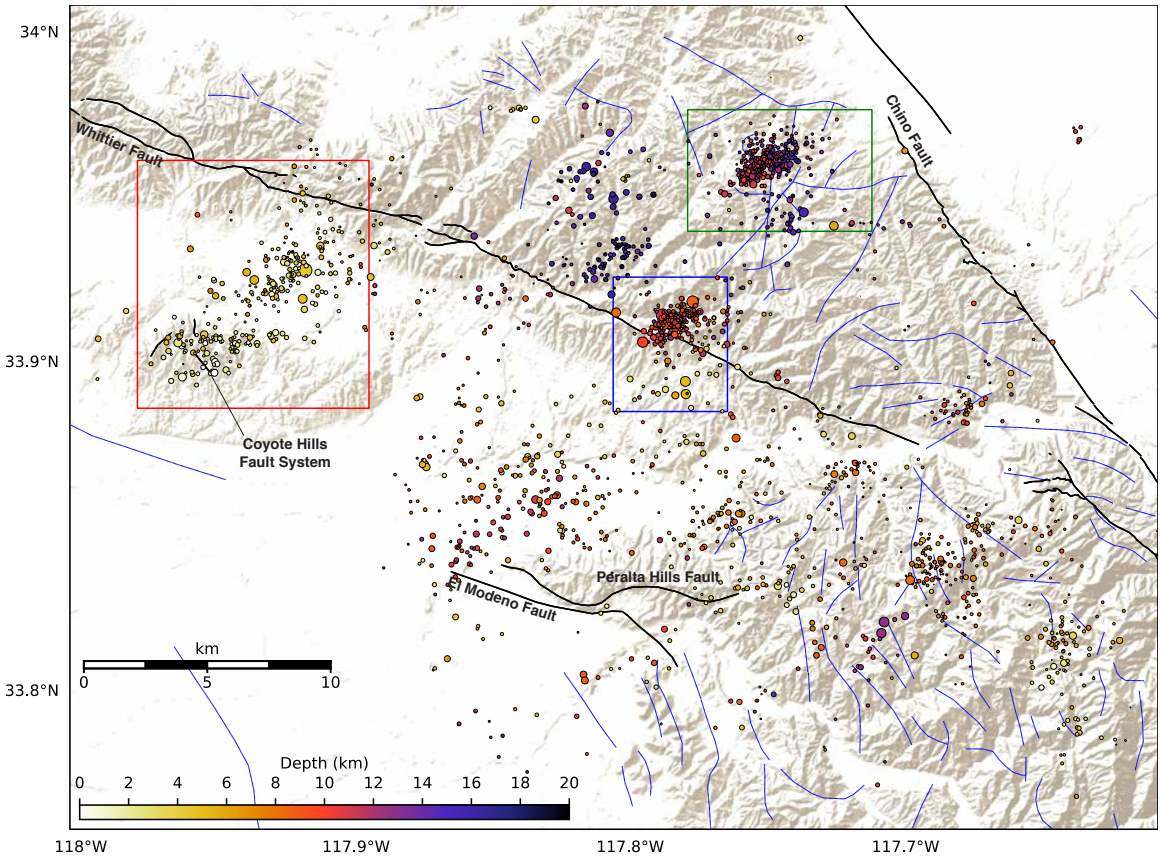

Figure 106: Map of the relocated locations of events shown in Figure 103 using a 0.2 differential travel time residual and the IASP91 Velocity Model (Figure 23b).

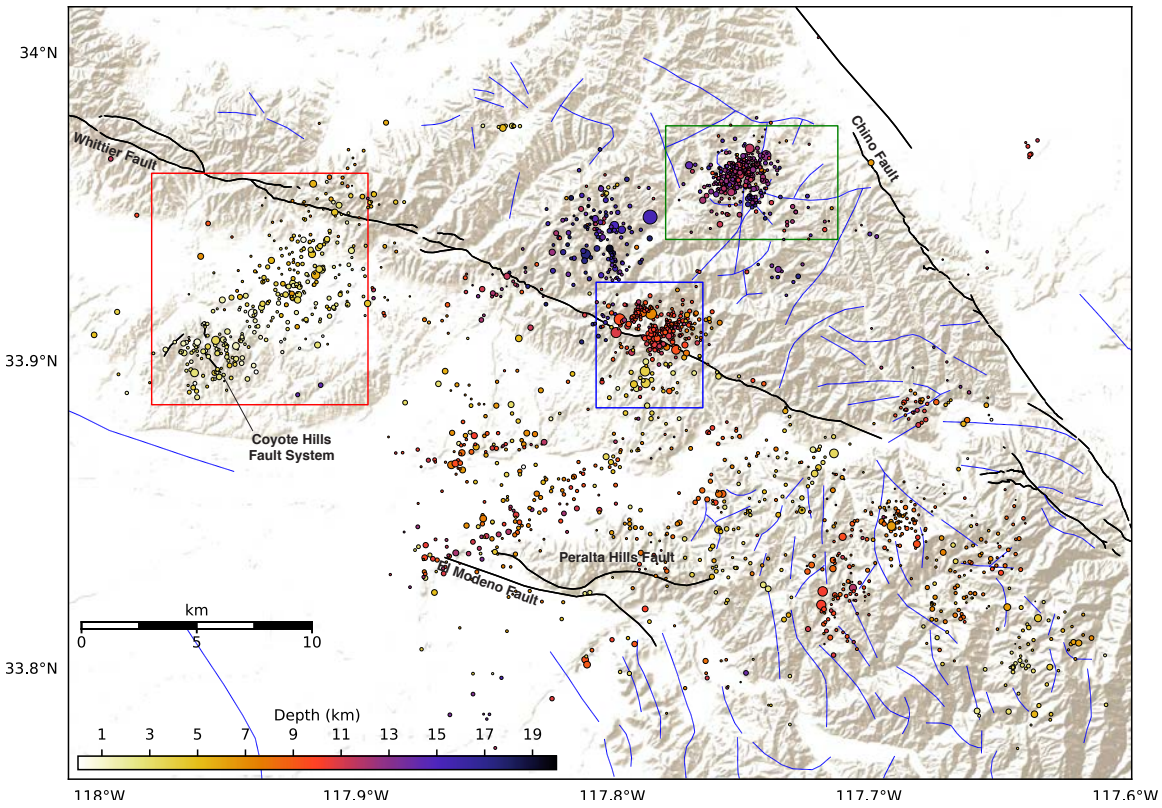

Figure 107: Map of the relocated locations of events shown in Figure 104 using a 0.2 differential travel time residual and the Smoothed Southern California Velocity Model (Figure 23b).

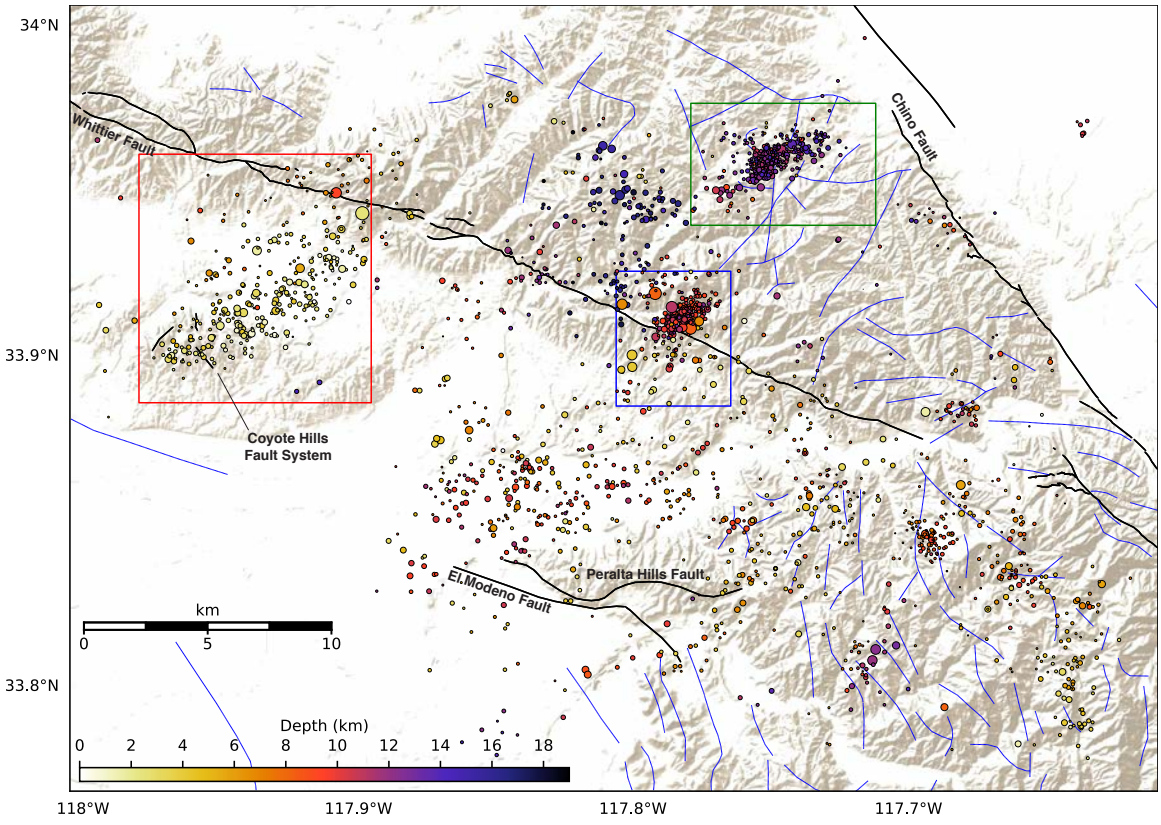

Figure 108: Map of the relocated locations of events shown in Figure 105 using a 0.2 differential travel time residual and the 1987 Whittier Narrows Earthquake velocity model (Figure 23b).

6.3 Appendix C: Original Event Locations for Each Velocity Model Relocation Results with a 0.6 RMS Differential Travel Time Residual

Shown below are maps of all original locations of events that were to be relocated using the three different velocity models under a 0.6 RMS differential travel time residual parameter used in this study. Figures 109, 110, and 111 show the original event locations the IASP91, for the smoothed southern California and Los Angeles Basin velocity models , respectively.

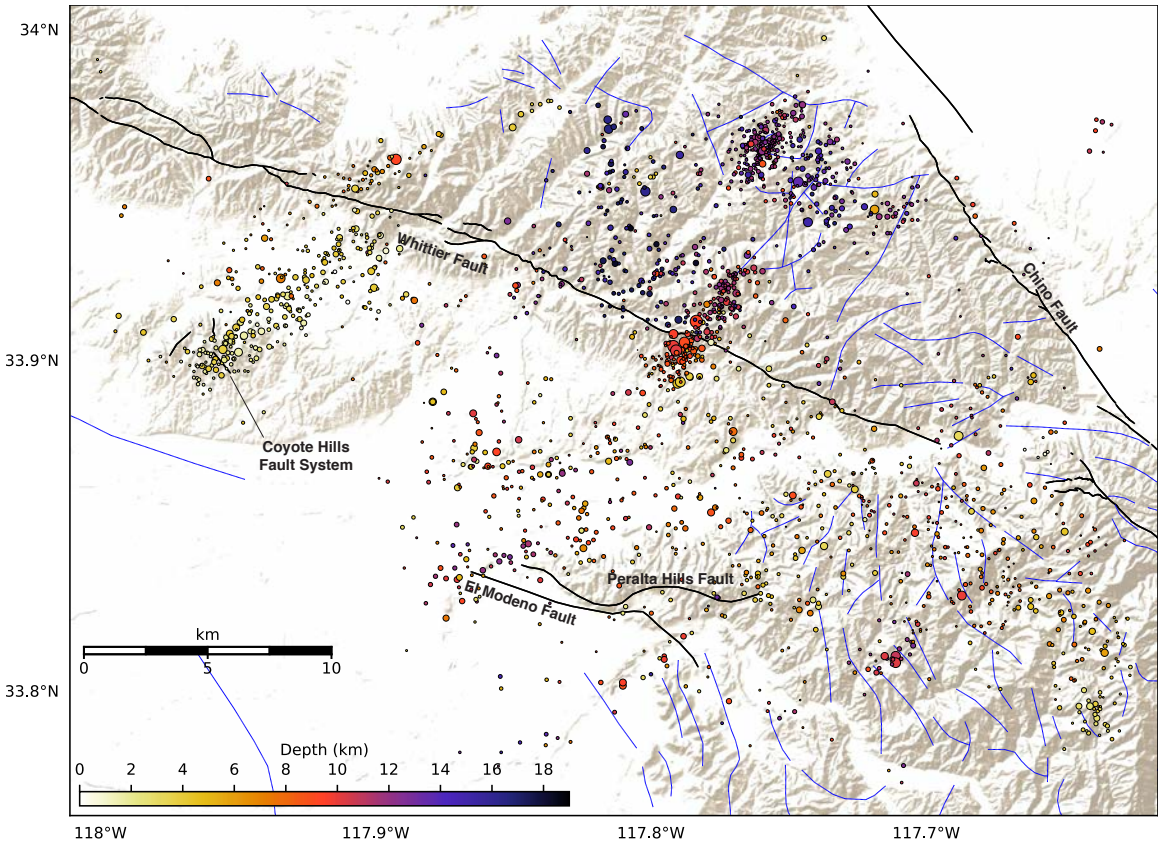

Figure 109: Map of the original events of events shown in Figure 112 using a 0.6 differential travel time residual and the Smoothed Southern California Velocity Model (Figure 23a).

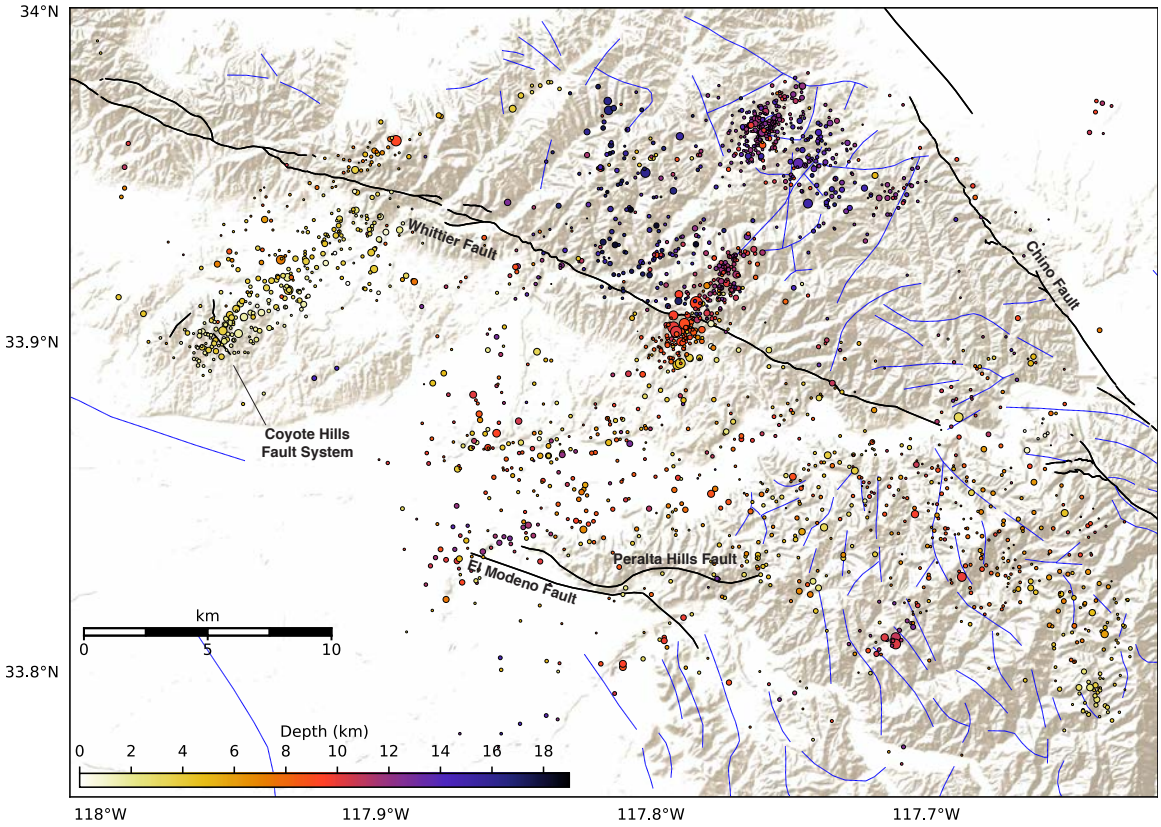

Figure 110: Map of the original events of events shown in Figure 113 using a 0.6 differential travel time residual and the Smoothed Southern California Velocity Model (Figure 23b).

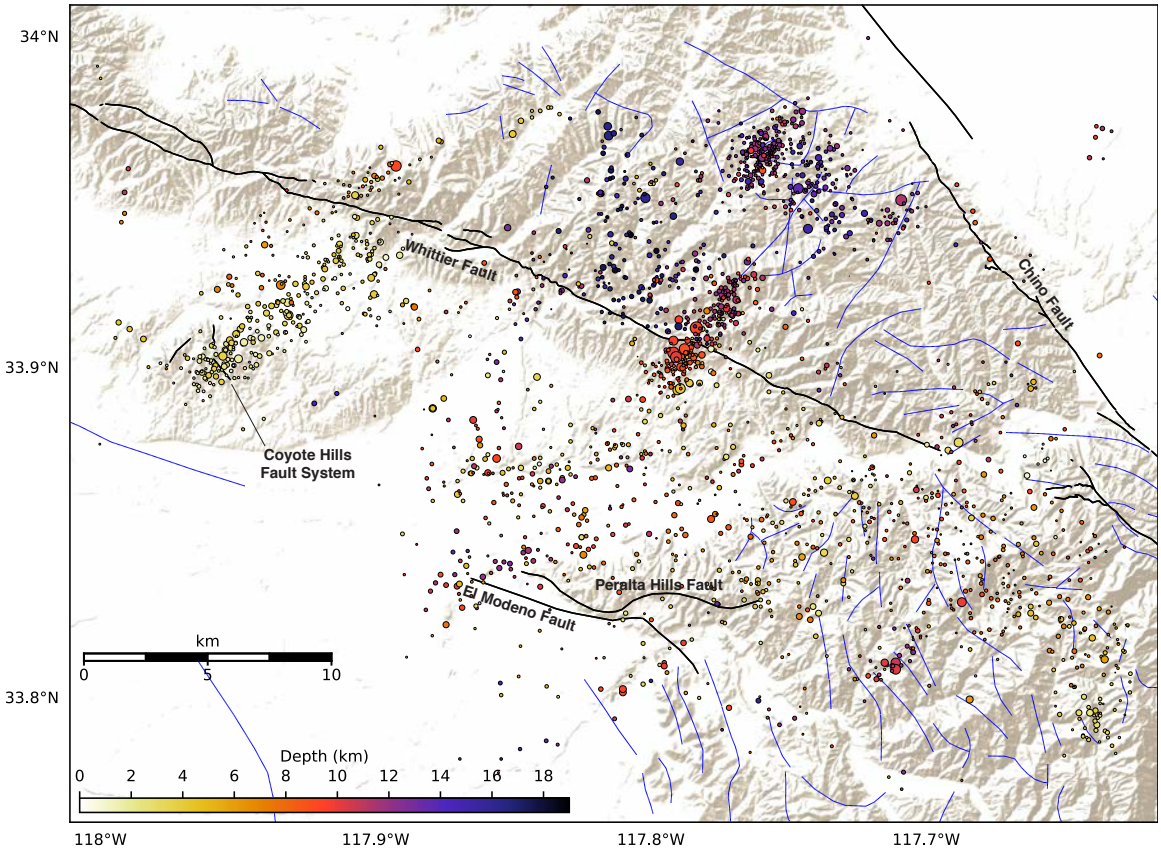

Figure 111: Map of the original events of events shown in Figure 114 using a 0.6 differential travel time residual and the 1987 Whittier Narrows Earthquake Velocity Model (Figure 23c).

6.4 Appendix D: Relocated Event Locations for Each Velocity Model Relocation Results with a 0.6 RMS Differential Travel Time Residual

Shown below are maps of all relocated event locations of events using the three different velocity models under a 0.6 RMS differential travel time residual parameter used in this study. Figures 112, 113, and 114 show the original event locations the IASP91, for the smoothed southern California and Los Angeles Basin velocity models , respectively.

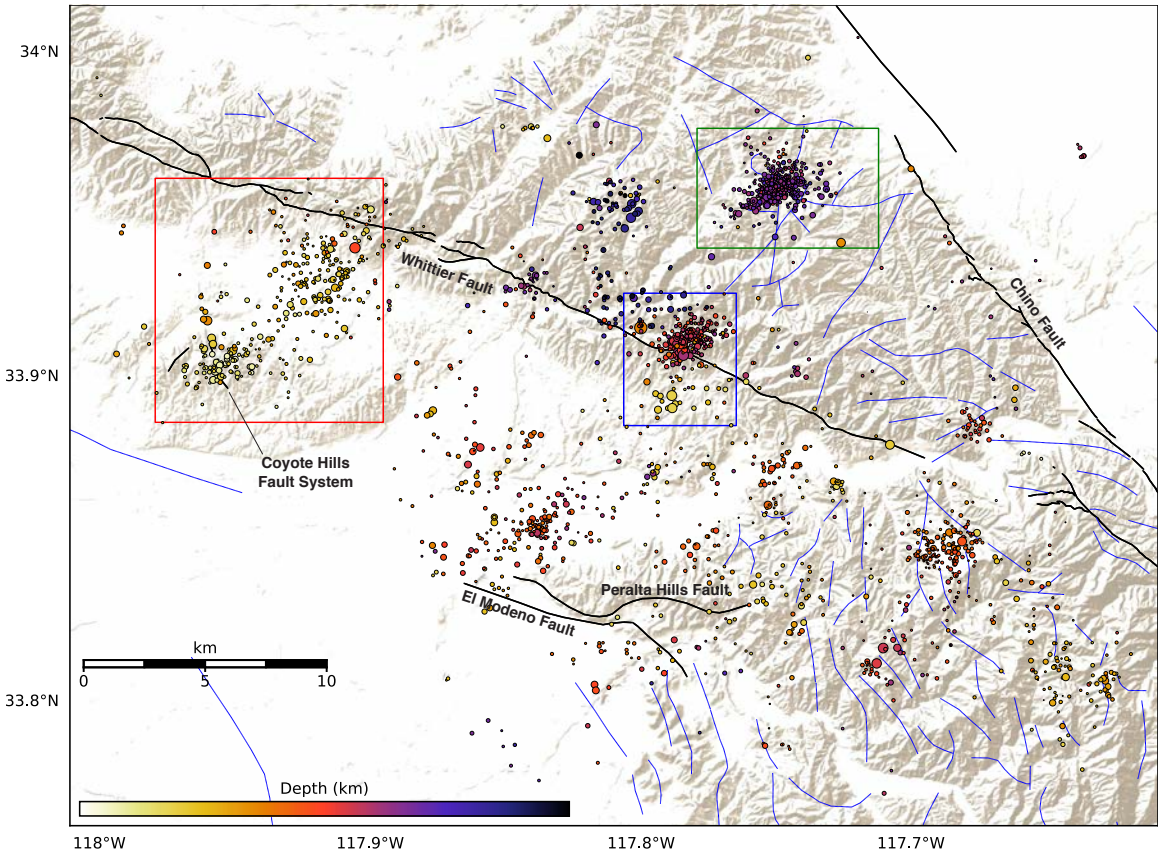

Figure 112: Map of the relocated locations of events shown in Figure 109 using a 0.6 differential travel time residual and the IASP91 Velocity Model (Figure 23b).

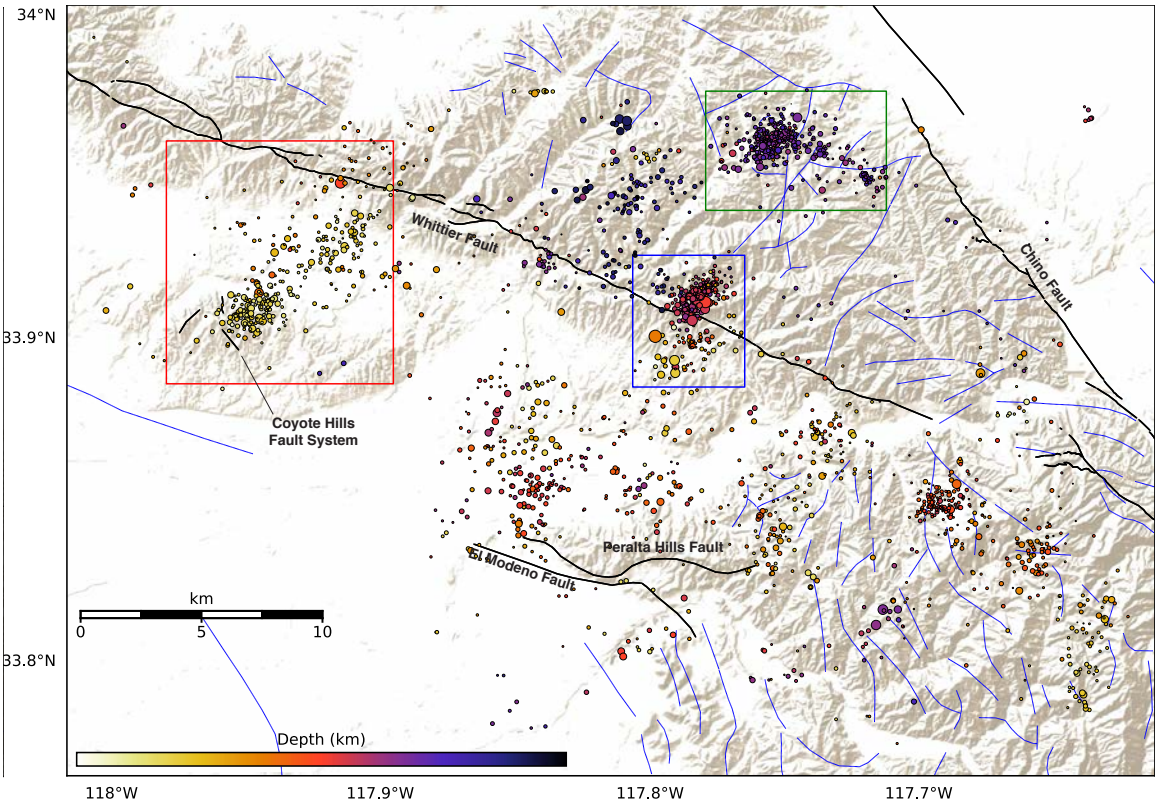

Figure 113: Map of the relocated locations of events shown in Figure 110 using a 0.6 differential travel time residual and the Smoothed Southern California Velocity Model (Figure 23b).

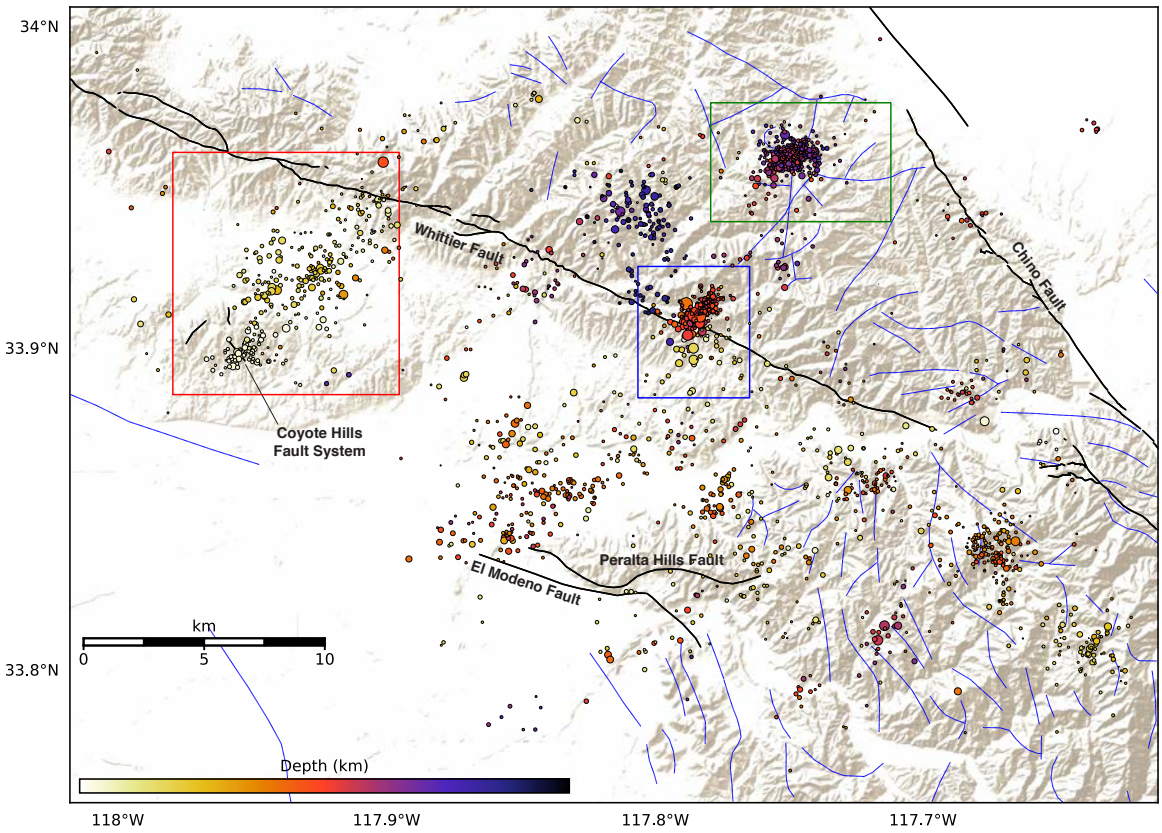

Figure 114: Map of the relocated locations of events shown in Figure 111 using a 0.6 differential travel time residual and the 1987 Whittier Narrows Earthquake velocity model (Figure 23b).